

ScienceDirect



IFAC PapersOnLine 54-16 (2021) 430-437

Pisciform Locomotion of an Improved Modular Biolocomotion Emulator

Khanh Q. Nguyen*, Craig A. Woolsey†, Raju V. Datla‡, Uihoon Chung**, and Muhammad R. Hajj ††

*,† Aerospace & Ocean Engineering, Virginia Tech,
Blacksburg, VA 24061 USA

†,**,†† Civil, Env., & Ocean Engineering, Stevens Institute of
Technology, Hoboken, NJ 07030 USA
*knguyen1@vt.edu, †cwoolsey@vt.edu,

†rdatla@stevens.edu, **uchung@stevens.edu, †† mhajj@stevens.edu

Abstract: This paper presents an experiment conducted to study the pisciform locomotion of an improved modular biolocomotion emulator in which the hydrodynamic and kinematic data are collected as the device mimics the body shape of real fishes in swimming action while being towed along a water tank at a steady speed. The results not only provide insights on how to select the optimal morphologies and locomotion gaits for such a biomimetic device but are also used to validate different proposed reduced-order model of the unsteady flow for the rapid development of future underwater autonomous vehicle.

Copyright © 2021 The Authors. This is an open access article under the CC BY-NC-ND license (https://creativecommons.org/licenses/by-nc-nd/4.0/)

Keywords: Hydrodynamics, biolocomotion, thrust, propulsive efficiency, towing basin, modular

1. INTRODUCTION

Over the years, the use of autonomous underwater vehicle (AUVs) and remotely operated vehicles (ROVs) in replacing human to carry out dangerous tasks in marine environment has become more popular. Although AUVs and ROVs operate underwater, many of them are controlled and propelled by man-made a system of propeller(s), which limits their performance and operational effectiveness in many ways (Mason and Burdick, 2000). From the biological standpoint, species of fish and marine animals are excellent swimmers with thousand years of natural evolution. Therefore, the aquatic robots that implement such a bio-inspired propulsion and control system are believed to possess better capabilities for speed, agility, robustness, and efficiency compared to those conventional propeller-based vehicles. For example, an early experiment conducted by Anderson et al. (1998) concluded that a mechanical tuna robot was able to reduce the drag on its body while being towed at a constant speed by undulating (flapping) the tail segment attached to its main body. In order to take advantage of these observations, an accurate and reliable dynamic model to estimate the hydrodynamic forces resulted from different types of locomotion of fishes and fish-like robots must be determined and validated.

The steady swimming motion of fish can be classified into a few different modes based on how much of its body is undulated to generate thrust during the swimming action. For example, boxfish and torpedo ray use "ostraciiform", which only involves in the back and forth oscillating of the caudal fins (comprised less than 10% of their body length). As a larger portion of the body is utilized, the locomotion types become ""thunniform (10-30% of body length) observed on tuna; "carangiform" (30-50% of body length) observed on jacks, mackerel; "subcarangiform"

(50-85% of body length) observed on cod, trout and finally; "anguilliform" (above 85% of body length) observed on eels or snakes (Webb, 1975).

For a given body shape and locomotion type, many experimental and theoretical studies have shown that the resulted thrust and propulsive efficiency are strongly related to the Strouhal number (Murray and Howle, 2003; Read et al., 2003). At a low St number, the flapping motion of the tail produce a classic "Benard-von Karman" (BvK) vortex street in the wake, which induces a net drag on the body rather than thrust. However, this vortex pattern can transition to "reversed Benard-von Karman" (rBvK) with the increase of either flapping amplitude (Triantafyllou et al., 1991) or frequency (Koochesfahani, 1989; Eloy, 2012), which also results in a higher St number. This phenomenon induces a jet at the centerline that push on actuated body and thrust is hence generated as a reaction force to the fluid momentum. The amount of thrust resulted from the locomotion generally increases with the St number but the propulsive efficiency for most swimming fishes peak in a narrow interval 0.25 < St < 0.35(Triantafyllou et al., 1993) across the entire undulatory locomotion spectrum. This optimal interval of St number will be the focus of the experiments conducted and presented in this paper.

The modeling of pisciform locomotion is highly non-linear and time-varying. In order to develop control method for a biomimetic device, the hydrodynamic model must be robust and have the capability to be integrated with a geometric control framework. High-fidelity model such as CFD is more capable in predicting the hydrodynamic performance of such a device. However, due to the immense computational power required, it is not a good tool for designers to rapidly explore a high-dimensional space of

design parameters. Instead, many have been relying on the reduced-order, quasi-steady flow models (Lighthill, 1971; Theodorsen and Mutchler, 1935; Tytell and Lauder, 2004; Weihs, 1989) early in the design cycle even though they often fail to capture the unsteady effects that play critical roles in the propulsion mechanism such as the the roll up of vortex rings shed by the tail movement and their evolution with time.

Having an experimental apparatus that is easy to be reconfigured and serves as a test platform to collect the forces resulted from different gaits and morphologies selection is critical in designing such a bio-inspired robot. Therefore, this paper presents the planning process and the results of how such an experiment can be conducted using an improved modular biolocomotion emulator (IMBE) to obtain and archive the hydrodynamic forces resulted from different pisciform locomotion. The IMBE is the second generation of a similar device introduced in (Beardsley et al., 2018) with numerous improvement made to expand its capability to achieve motions with higher flapping frequency and represent higher undulatory modes with more modules. The main focus of this experimental effort is to generate hydrodynamic data that can be used for flow model validation but it also provides preliminary analysis and interpretation of the results.

2. EXPERIMENT SETUP

2.1 IMBE Test Article

The test apparatus used in this experiment is the *improved* modular biolocomotion emulator, which is a second generation that evolves from one introduced in (Beardsley et al., 2018). The IMBE configuration chosen for the test campaign consists of five rigid modules, each with a servo embedded inside and a head fairing. The CAD model the the fully assemble IMBE device is shown Figure 1. The position of these servos and hence, the angle of each module relative to the centerline, can be controlled independently. In fact, this is how the device approximate different mode of pisciform locomotion. During steady swimming state, the fish body always exhibits a certain shape that can be represented as a waveform passing from its head to tail (Lauder and Tytell, 2005). By commanding the servos to oscillate in a synchronous pattern, we can approximate the overall shape of the locomotion waveform as if each module acts like a "penducle" between the head and tail fin.

The modules that make up the IMBE is designed to be interchangeable so that one could add or remove to represent different undulatory regime from carangiform to anguilliform. Each module houses a Hitec D956WP steelgear, IP67-rated waterproof servo capable to produce a max torque of 405 oz.in with a slew rate of 60° in 0.13 seconds. Compared to the previous generation, IMBE has less electronic components with only the servo and the wires connected them to the control circuit board getting submerged along with the device during operation. This helps to reduce the possible point of failures and the overall weight of the device. When the device actuated underwater, it is powered by a 7.4 VDC supply mounted on the towing carriage.

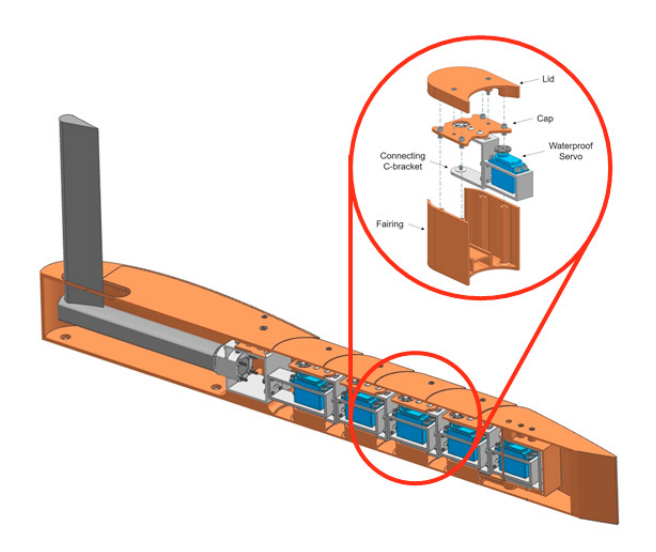


Fig. 1. CAD rendering of the fully assemble IMBE device

The fairing for each module is made from 3-D printed ABS material with minimum wall thickness for structural support, leaving the internal space open for free-flooding of water. The overall geometry of the IMBE retains the design language from its predecessor with the forebody fairing made up 70% of the NACA 0024 hydrofoil and the tail made up the other 30%. These fairings help to improve the flow quality over the device while still allow the modules to rotate at maximum $\pm 20^{\circ}$ relative to each other. During the experiment, the entire device is connected to an L-shape 6DOF balance through a metal collar inside the forebody module, which help to measure the axial and side force component $(F_x, F_y \text{ respectively})$. Figure 2 shows a top-view schematic with detail dimensions of the modules and their center-of-rotation. The angle θ_i of each module is calculated from the input motion parameter and the output torque τ_i generated by each servo is recorded.

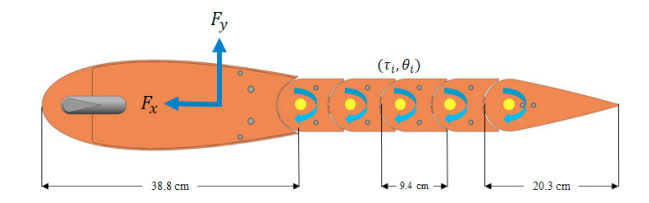


Fig. 2. Top-view schematic of IMBE with detail dimensions

2.2 Test Facility

The test campaign is conducted in a towing tank available in Davidson Laboratory at Stevens Institute of Technology. The tank is 313 feet long, 16 feet wide and can support a water depth of up to 8 feet. The carriage sitting on top of the tank is capable of reaching towing speed up to 100 ft/s with a precise control of 0.01 ft/sec in speed increment. The low uncertainty is critical for the experiment since its objective is to achieve different discrete values of Strouhal number. The size of the tank helps to minimize wall effects from the waves generated by the towing action. During the experiment, the IMBE and the L-shape sting balance are mounted to the carriage arm that extends closer to the

water surface while the supported equipment need to control the device and collect hydrodynamic data are secured to the carriage platform above the waterline. Pictures of the setup and the IMBE in action are shown in Figure 3.

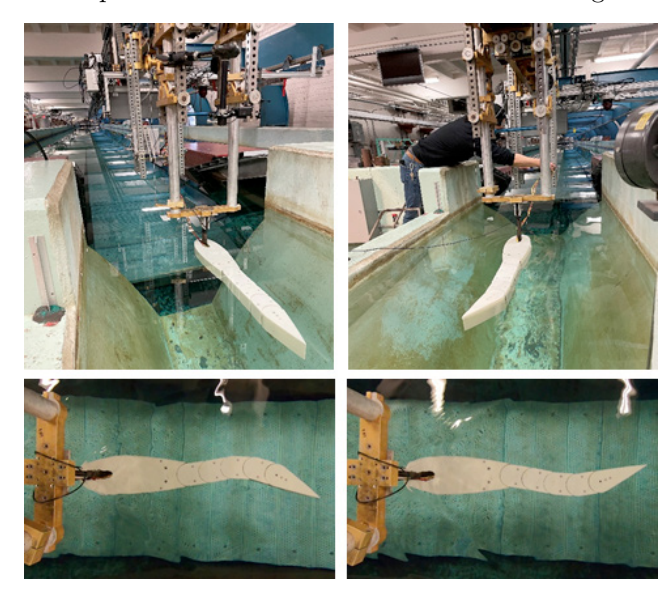


Fig. 3. Top: IMBE mounted under the towing carriage Bottom: IMBE in action during the experiment

2.3 Motion Control & Data Acquisition System

To mimic the swimming action of fishes, the IMBE uses the available modules to approximate an oscillating waveform as it is towed through the water at a certain speed. The shape of the waveform and the amplitude envelope can be defined by a few parameters (usually referred to as gaits), including the max wave amplitude (typically occurs at the trailing edge), the flapping frequency, the phase shift angle of the waveform and the geometry of the apparatus (such as the length of each module and the total number of modules). A LabVIEW virtual instruments (VI) program is written to receive these inputs and calculate the position at which each servo is supposed to be in real time and send out the command. A summary of the required inputs and outputs of the experiment can be found in Table 1. During the experiment, two separate system are used to control the motion of the IMBE and collect hydrodynamic and kinematic data.

Input Gaits	Output Data		
Number of modules, N	Axial forces, F_x		
Length of each modules, L_i	Side forces, F_y		
Max waveform amplitude, A	Yaw moment, M_z		
Flapping frequency, f	Servo output torque, τ_i		
Waveform specific parameter(s)	Servo true position, θ_i		
Target tow speed, U_{∞}	True tow speed, U_{∞}		

Table 1. Summary of inputs and outputs

First, all the servos inside the modules are connected to a control circuit board. The board receives the 5.0 VDC power from a stand-alone power supply and delivers it to each servo. There is also a Teensy 3.2 microcontroller on the board that serves as the interface between the servos and the LabVIEW motion control VI. The microcontroller is programmed to receive the serial command from the

LabVIEW VI and send out individual command to each servo to rotate to the desired position. It also receives the down-link data from the servos, which contain the information of the true position and the drawn current by each servo (measured with the ACS712 current sensor onboard), and then transfers the data package to the LabVIEW VI. Prior to being place inside the module, the output torque by each servo is calibrated with the amount of current it draws. Therefore, as the VI receives the downlink package, it can interpret the kinematic data and plot the output torque along with the true motion of the device on the VI graphical interface in real-time.

Meanwhile, the hydrodynamic data is obtained using the 6DOF SB100 sting balance manufactured by Modern Machine & Tool Co. A series of strain gauges are placed on the cylindrical part of the balance such that the resulted strains are proportional to the forces applied. Therefore, the forces and moments resulted from the IMBE locomotion can be determined by measuring these output strains. In order to do this, balance is connected to the Vishay 2310-Series Signal Conditioning and Amplifier, which has a Wheatstone bridge circuit inside. The bridge circuit excites the strain gauges at 3.5 VDC and measures the output voltages with active filtering applied. The analog signals of these output voltages are then recorded by a National Instruments (NI) myDAQ at a sampling rate of 250 Hz and converted to the hydrodynamic forces with a known calibration factor. In addition, the balance is used as a support structure that allow the IMBE to be mounted to the towing carriage during the experiment.

It was our intention to record both of the axial and side forces produced by the IMBE during the course of the test campaign. However, as the experiment concluded, we determined that only one signal conditioning & amplifier device that measured the axial force functions normally during the experiment. Therefore, only results of the axial force F_x are reported in this paper. A diagram that summarizes how all the equipment are set up is shown in Figure 4.

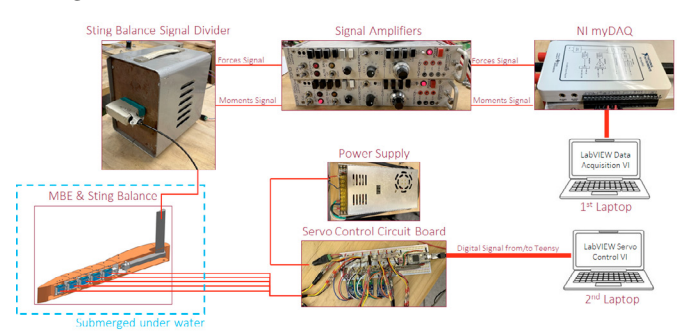


Fig. 4. Equipment setup diagram for the experiment

2.4 Test Matrix Consideration

From the observations of the midlines and outlines of different fish species reported in Lauder and Tytell (2005), the best waveform to approximate the fish body shape during steady state of swimming is an exponential sinusoidal with the following wave equation:

$$y(x,t) = A\left(\frac{e^{kx} - 1}{e^{kL} - 1}\right)\sin(\omega x + ut + \phi) \tag{1}$$

where x and y are Cartesian coordinate of the tail in a topdown view with the fish head located at the origin (0,0)with the fish body extended along the positive x-axis and k is the "exponential constant" that can either advance or delay the growth of the amplitude toward the tail. In addition, we also consider the case where the amplitude envelope of the waveform is the modeshape of a cantilever beam with the overall length L equal to the body length of the fish. The wave equation of this gait is:

$$y(x,t) = AY_r(x)\sin(\omega x + ut + \phi) \tag{2}$$

where the function $Y_r(x)$ is modeshape equation and can be found by solving the Euler-Bernoulli cantilever beam bending for a particular mode (1st, 2nd, etc.) This is a part of our effort to investigate whether or not the modeshape body outline produces any kind of resonant effect to the thrust generated from the motion. The body midlines and overall outlines of the two waveforms approximated by the IMBE for this experiment are shown in Figure 5. The variable ω and u in equation 1, 2 are the spatial frequency and velocity, respectively. In order to achieve a meaningful shape illustrated in Figure 5, their values are set to be a function of the geometry of the apparatus as:

$$\omega = \frac{2\pi}{NL_i}$$
 and $u = -2\pi f$ (3)

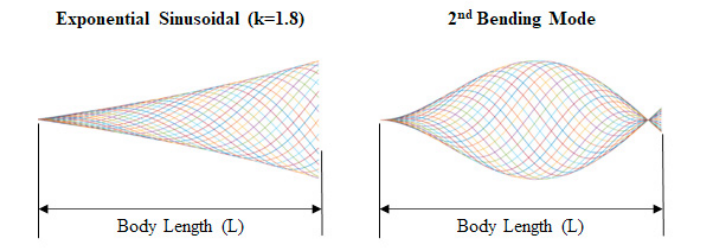


Fig. 5. Waveforms that represent the fish outlines and midlines to be approximated for the experiment

One of the main objectives of the experiment is to determine the propulsive efficiency of different locomotion modes of such a fish-like robotic device . However, since the IMBE is a towed apparatus, we adapt the approach proposed by Maertens et al. (2015) to estimate the quasi-propulsive efficiency of a self-propelled device under towed condition. For each waveform, the following test cases are considered:

- Case 1 The IMBE is not actuated but towed at different speeds.
- Case 2 The IMBE is actuated at different flapping frequencies and waveforms but remains stationary (i.e. the carriage does not move forward).
- Case 3 The IMBE is actuated while the towing carriage moves forward at a steady speed U_{∞} to simulate free-stream flow encountered by a real fish.

The hydrodynamic forces obtained from test case 1 provide a correlation between the static body drag and the towing speed. Meanwhile, the measurements collected from different motions in test case 2 offer more insights about the relationship between the hydrodynamic & kinematic performance and the flapping frequency of the body. Finally, the quasi-propulsive efficiency of the locomotion can be derived using the following equation:

$$\eta_{QP} = \frac{(D + T_n)U_{\infty}}{P_{in}} \tag{4}$$

where T_n is the net forces resulted from the motion exhibited in test case 3 and D is the body drag of the unactuated IMBE (i.e. the resistance of a "dead fish") at the selected tow speed U_{∞} for that particular run, which can be derived or interpolated from test case 1.

The values of input gaits for each waveform type across all the test cases are summarized in Figure 6 although it is organized specifically for test case 3 to study the change in propulsive efficiency with the change in flapping frequency, tow speed, at different Strouhal numbers. Changing the value of either flapping frequency f or tow speed U_{∞} results in different value of the Strouhal number for the motion. Each "dynamic" case in the test matrix shown in Figure 6 represents a specific combination of flapping frequency and Strouhal number for both waveforms. The tow speed is then calculated to achieve the targeted Strouhal number. The Strouhal number increases from 0.1 to 0.4 going down the row of the dynamic case. In addition, each column represent a tier of the tow speed for each Strouhal value. Going across the dynamic case column from left to right, the tow speed gradually increase. By structuring the gait values this way, meaningful conclusions can be drawn with a limited amount of trials (24 total for test case 3).

	Low To	Low Tow Speed		Tow Speed	High Tow Speed	
	Dynamic 1		Dynamic 3		Dynamic 6	
Parameters	Exp Sine	2nd Mode	Exp Sine	2nd Mode	Exp Sine	2nd Mod
St Number	0.10		0.10		0.10	
Frequency (Hz)	0.75		1.00		1.25	
Amplitude (cm)	5.00	5.50	5.00	5.50	5.00	5.50
Tow Speed (m/s)	0.38	0.41	0.50	0.55	0.63	0.69
	Dynamic 2		Dynamic 5		Dynamic 9	
Parameters	Exp Sine	2nd Mode	Exp Sine	2nd Mode	Exp Sine	2nd Mod
St Number	0.20		0.20		0.20	
Frequency (Hz)	1.00		1.25		1.50	
Amplitude (cm)	5.00	5.50	5.00	5.50	5.00	5.50
Tow Speed (m/s)	0.25	0.28	0.31	0.34	0.38	0.41
	Dynamic 4	Dynamic 8		Dynamic 11		
Parameters	Exp Sine	2nd Mode	Exp Sine	2nd Mode	Exp Sine	2nd Mod
St Number	0.30		0.30		0.30	
Frequency (Hz)	1.25		1.50		1.75	
Amplitude (cm)	5.00	5.50	5.00	5.50	5.00	5.50
Tow Speed (m/s)	0.21	0.23	0.25	0.28	0.29	0.32
	Dynamic 7	Dynamic 10		Dynamic 12		
Parameters	Exp Sine	2nd Mode	Exp Sine	2nd Mode	Exp Sine	2nd Mod
St Number	0.40		0.40		0.40	
Frequency (Hz)	1.50		1.75		2.00	
Amplitude (cm)	5.00	5.50	5.00	5.50	5.00	5.50
Tow Speed (m/s)	0.19	0.21	0.22	0.24	0.25	0.28

Fig. 6. Summary of input gaits values for the experiment

For test case 1, the IMBE is towed at the speeds indicated in dynamic 1 to 9 (18 test runs in total since each dynamic case has 2 waveform types and hence 2 associated speeds). For test case 2, the IMBE is actuated at a flapping frequency ranges from 0.75 Hz to 1.75 Hz at an increment of 0.25 Hz for each waveform type. The max amplitude A is kept constant between the test runs and are chosen to be 5.0 cm for the exponential sinusoidal waveform and 5.5 cm for the $2^{\rm nd}$ bending mode to keep the relative angle of the modules within the design limit. In total, there are 10 test runs for case 2.

2.5 Uncertainty Analysis

The uncertainties of the axial forces reported in Section 3 are calculated for each motion using the standard de-

viation (σ) of the force dynamic response. During each run, the IMBE is actuated for at least 30s but only a snapshot of 20s of the hydrodynamic data (where the motion is steady) is used for the analysis. The force signal is recorded at a rate of 250 Hz, which yields 5,000 samples. The measurement uncertainties of the mean axial forces from the experiment are

$$\delta(\bar{F}_x) = \pm \frac{2\sigma(F_x)}{\sqrt{M}} \tag{5}$$

where M is the total number of samples. The $\pm 2\sigma$ -range corresponds to a 95% confidence interval for the reported values. Then, the uncertainty of the quasi-propulsive efficiency are derived from the measurement uncertainties of the forces T_n, D , tow speed U_{∞} and input power P_{in} .

3. EXPERIMENT RESULTS AND DISCUSSION

3.1 Body Drag Measurement

The body drags of the unactuated IMBE configuration at different towing speeds are shown in Figure 7. Using least-square fit, a quadratic regression between the two quantities is found to be:

$$D = 1.3791U_{\infty}^2 \tag{6}$$

This correlation is used to calculate the resistance of a "dead fish" D in determine the quasi-propulsive efficiency of the IMBE motion (equation 4) in test case 3. Unlike empirical models that used to predict the true thrust and drag produced by the undulating motion of fish such as Lighthill's Elongated Body Theory (Lighthill, 1971), it is difficult to distinguish between these two force components and measure them separately for a self-propelled system. Instead, the IMBE is towed at a known speed to measure the net force produced by the actuated motion to determine whether or not it can over the least resistance force in which the device encountered in the undeformed configuration being propelled by a conventional method (propellers, pump jet, etc.).

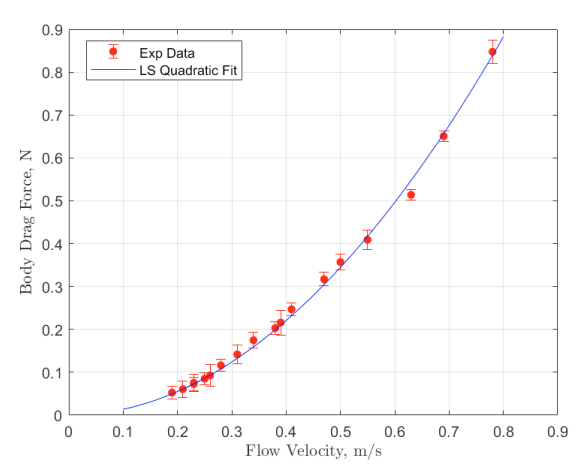


Fig. 7. Body drag forces of the unactuated IMBE at various towing speeds

3.2 Dynamic Force Measurement

The mean values of the axial force (thrust) recorded over a period of 10s where the motion of the IMBE is steady for the two waveforms at different frequencies in test case 2 are shown in Figure 8 along with the uncertainties of the measurements. Note that for this test case, the carriage remains stationary during the motion so the device is not towed and the flapping frequencies are increased from 0.75 Hz to 1.75 Hz at an increment of 0.25 Hz for each waveforms. Overall, the thrust generated by both waveforms increases with the flapping frequency f but at different rate. At a low value of f, both waveforms produce about the same amount of force but as the frequency increases beyond 1.25 Hz, the $2^{\rm nd}$ bending mode produces significantly more thrust compared to the exponential sinusoidal waveform with a higher rate of marginal gain.

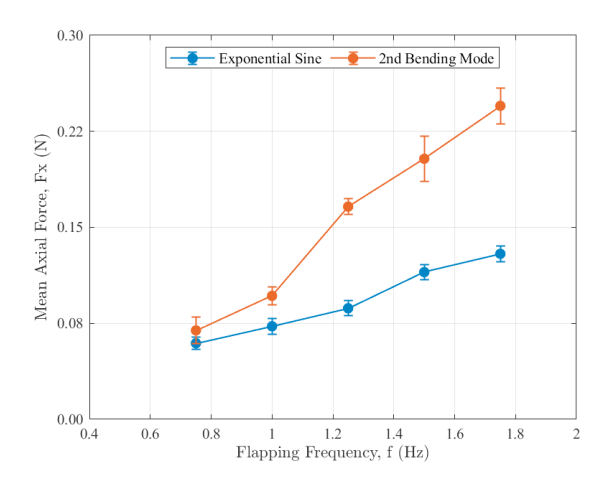
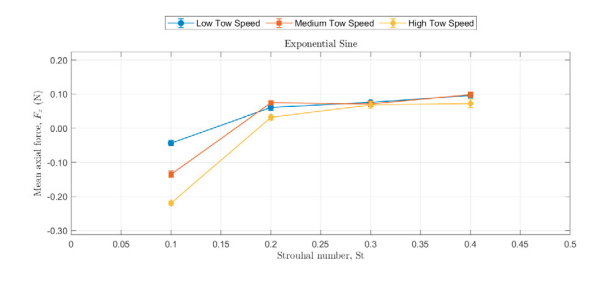


Fig. 8. Mean axial forces produced by different motions of IMBE in the absence of free-stream flow (test case 2)

Meanwhile, with the presence of free-stream flow in test case 3, the resulted axial forces from the motion exhibited by the IMBE also change. From Figure 9, note that at a low Strouhal number, which corresponds to a higher tow speed within that speed setting as seen in the test matrix (Figure 6), the measured axial forces on both waveforms are negative, meaning that the motions do not generate enough thrust to overcome the drag on the deformed body. However, as the tow speed is reduced and the flapping frequency increases, which lead to the increment of Strouhal number for the motion, the IMBE experiences less body drag and the actuation of its modules starts to generate a positive mean axial force. From the observations made in test case 2, one would expect that the mean axial force would be proportional to the Strouhal number. However, this behaviour is only observed on the 2nd bending mode waveform at low and medium tow speed setting. Otherwise, after a significant gain going from the Strouhal number of 0.1 to 0.2, the mean axial forces either plateau or only increase at a marginal rate.

Plotting the mean axial force between the two waveforms for each tow speed setting (Figure 10), we observe that at low tow speed, 2nd bending mode waveform register a higher force measurement with the increase of flapping frequency and Strouhal number compared to the exponential sinusoidal one. However, at high tow speed setting, this trend is reversed as the exponential sinusoidal motions can sustain a positive mean axial force while the 2nd bending mode motions result in negative net forces except for the case where Strouhal number equal to 0.4.



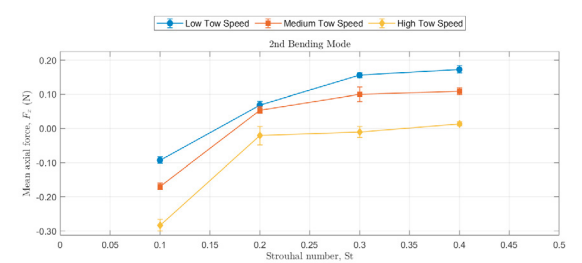


Fig. 9. Mean axial forces produced by the IMBE motion in towed conditions (test case 3) for each waveform

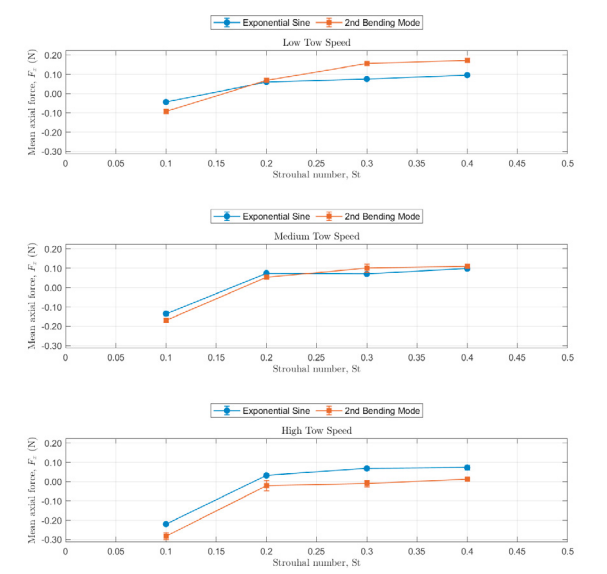


Fig. 10. Mean axial forces produced by the IMBE motion in towed conditions (test case 3) at each speed setting

As mentioned earlier, the undulating motion of the IMBE modules generates a pattern of reversed Benard-von Karman (rBvK) vortices in the wake, which induced a jet flow in the free-stream flow direction that results in a net thrust on the body. The magnitude of the generated thrust depends on the frequency and the strength at which these vortices are formed and their proximity to the trailing edge of the IMBE as they shed from the tail module (Quinn et al., 2014). In the absence of the free-stream flow as in test case 2, the rBvK vortices naturally traverses down the body length of the device and remain in the wake for longer. Therefore, the magnitude of the thrust generated is higher compared to the motions in test case 3. The overall shape of the actuated IMBE also give some insights to explain the differences in thrust generated between the two waveforms. From Figure 5, the body shape reach the max amplitude half way through the body length on the 2nd bending mode waveform instead of at the tail on the exponential sinusoidal waveform. As a result, the relative angles between the modules to produce the 2nd bending mode waveform are higher, which lead to the formation of stronger rBvK vortices earlier along the body shape. Therefore, when the IMBE is stationary or tow at low speed, these vortices remain in a close vicinity of the tail module and produce a higher propulsive force on the body compared to the exponential sinusoidal waveform.

However, for the 2nd bending mode, the IMBE also protrudes a larger portion of its body into the free-stream flow. The high angle of the modules relative to the free-stream might lead to flow separation from the body at high Reynolds number that would cause a rise in drag. Therefore, as the tow speed increases, the benefit from this waveform type starts to diminish. Although the exponential sinusoidal waveform actuation generates less thrust in test case 2, its streamline shape reduces the amount of drag experienced by the body results in a higher net force.

Meanwhile, the marginal gain of thrust observed on both waveforms beyond the Strouhal number of 0.2 within each speed setting is interesting. This phenomenon might be due to either the faster oscillating motion might shed the vortices in a higher frequency but with a weaker strength or the drag generated from the increase of flapping frequency might be substantially more than the gain of thrust. This supports the claim that there is a narrow range of Strouhal number where the locomotion is optimal.

3.3 Dynamic Torque Measurement

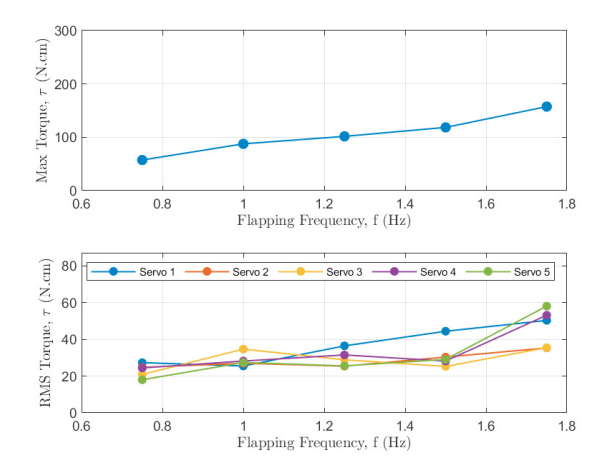


Fig. 11. Max and RMS torque of the servos for *exponential* sinusoidal waveform motions in test case 2

The maximum and root-mean-square (RMS) value of the output torques measured across the servos during the motions in test case 2 are shown in Figure 11 (for exponential sinusoidal waveform) and Figure 11 (for 2nd bending mode waveform). In general, the torque increases with the flapping frequency, both max and RMS value since the servos must move to the desired position faster. The motions of 2nd bending mode waveform require more torque compared to the exponential sinusoidal due to the large relative angles between the modules. With a few exceptions, the max RMS value of the torque is usually observed on the first servo since it has to move the most masses during the actuation.

The max output torque across all the servos for motion in test case 3 are shown in Figure 13. Across both waveform

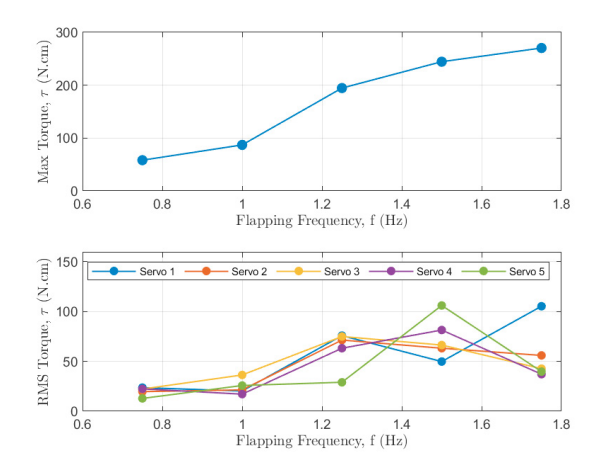
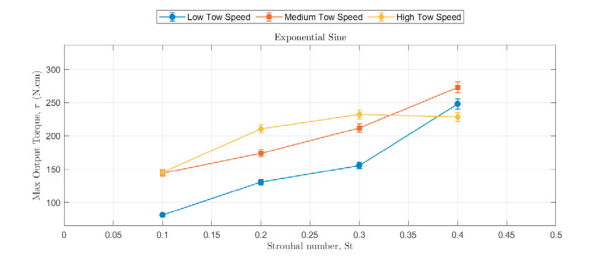


Fig. 12. Max and RMS torque of the servos for 2^{nd} bending mode waveform motions in test case 2



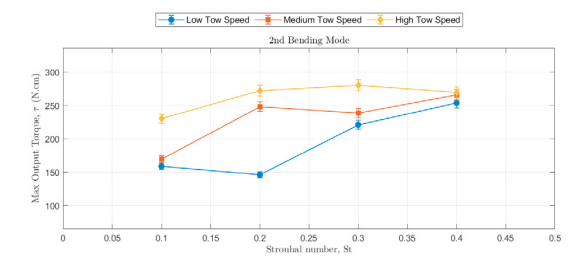


Fig. 13. Max output torque from the IMBE motions in towed conditions (test case 3) for each waveform

types, the max torque increases with the tow speeds, which is expected since the servos must work harder to overcome a stronger flow the modules encountered during the actuation. Within each speed setting, the max output torque generally increases with the flapping frequencies which is associated with a higher Strouhal number. However, for the 2nd bending mode waveform, there is a small range of Strouhal number where the the max torque does not follow this trend and remain constant. With a limited number of test runs, it is difficult to find the exact motion range for this behavior.

3.4 Quasi-Propulsive Efficiency

The hydrodynamic and kinematic data collected are used to compute the quasi-propulsive efficiency of the locomotion exhibited in test case 3 using equation 4. Plotting the results, we observe different qualitative trend between the two waveforms. From Figure 14, note that for the motions utilized the exponential sinusoidal waveform, the efficiency has already peaked at a Strouhal number outside the testing range for the low and high tow speed setting while for the medium speed setting, the locomotion reaches

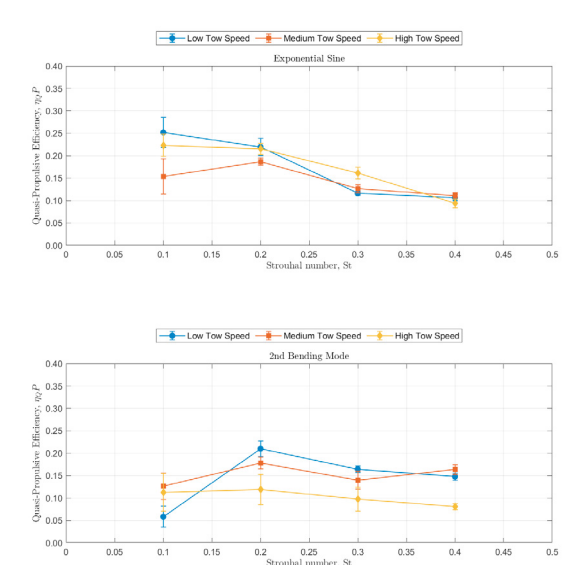


Fig. 14. Quasi-propulsive efficiency of the locomotions exhibited by the IMBE in test case 3 for each waveform

the optimal point around the Strouhal number of 0.2. This is also the Strouhal number where the 2nd bending mode locomotions achieve maximum propulsive efficiency across all tow speed settings. Beyond this range, the propulsive efficiencies of both waveform type gradually decline. From the previous section, it takes more power to sustain the actuation at a greater Strouhal number (due to the high flapping frequency associated) but the benefit of extra thrust is only marginal, which lead to the loss in efficiency.

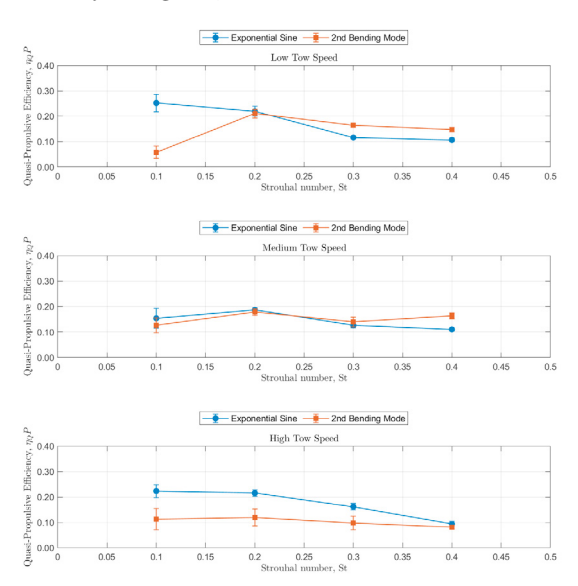


Fig. 15. Quasi-propulsive efficiency of the locomotions exhibited by the IMBE in test case 3 for speed setting

Plotting the efficiency of both waveform locomotions for each tow speed as seen in Figure 15, we observe that exponential sinusoidal waveform is more efficient at high tow speed setting. At low and medium speed, 2nd bending mode locomotions are better only at high Strouhal number. Recall from Figure 9, only motions that utilize the exponential sinusoidal waveform can sustain a positive net force in a high Reynolds number free-stream flow with a more streamlines body shape. Meanwhile, 2nd bending

mode locomotions are better in generating more thrust without the compromise in drag at a low Reynolds number. The resulted propulsive efficiency reflects the trend observed on the hydrodynamic performance of the device.

For the simplicity of the experiment, the IMBE device is towed instead of self-propels by the locomotions. The towed action still preserves the hydrodynamic nature of a steady swimming motion observed on fishes and provides meaningful data for underwater robotic gaits optimization. In many applications, the ultimate goal is to minimize the power consumption of the device for endurance capability, which correlates to the largest quasi-propulsive efficiency η_{QP} for a given self-propelled vehicle under towed conditions (Maertens et al., 2015). The data needed to compute η_{QP} are easy to obtain with standard equipment and therefore, help to simplify the experimental set-up and design challenges for the IMBE.

In the previous experiments that observes real locomotions of different fish species at various sizes, Eloy (2012), Triantafyllou et al. (1991) and Triantafyllou et al. (1993) all observed that these animals swim within a narrow range of optimal Strouhal number from 0.25 to 0.35. From our experiment, the quasi-propulsive efficiency of the IMBE under towed conditions peaks around the Strouhal number of 0.2 for most of the motions, which is not far from the true optimal range of fishes. The small discrepancies can be accounted by the rigidity of the modules that make up the IMBE, which can not mimic the flexible peduncles of the real fishes so the motion exhibited by the such a robotic device would have a different optimal performance.

4. CONCLUSIONS AND FUTURE WORKS

An improved version of the modular biolocomotion emulator (IMBE) is designed to mimic the pisciform locomotion types ranging from ostraciiform to subcarangiform. The IMBE is capable to undulate its linkages synchronously to approximate the natural body shape of a real fish in steady swimming action with the morphologies and gaits inputs specified by the user. To test the device capability, an experiment is carried out at Steven Institute of Technology towing tank that subjects the IMBE to a variety of locomotion types to collect hydrodynamic and kinematic data produced by its undulating motion. As the IMBE actuates the modules, it is towed along the tank at various speeds to represent different combinations of the Reynolds and Strouhal numbers. The optimal motion of the IMBE align well with the observations made by previous experimental efforts although a few unique discoveries are made for such a biomimetic device upon its hydrodynamic performance.

With promising results from the experiment, we plan to explore the locomotions with higher flapping frequency and undulating module. The data collected is used to enhance the design of future underwater robotic vehicles.

ACKNOWLEDGEMENTS

The authors kindly acknowledge the support of the National Science Foundation (NSF) under the Grant No. CMMI-1635143 and the staffs of Davidson Laboratory at Steven Institute of Technology for in facilitating the experiments. The authors also gratefully recognize the helps and

advisory provided by the following graduate assistants and colleagues throughout the design process of the apparatus: Ahmed Hussein, Brenton Morris, and Minh Vu.

REFERENCES

- Anderson, J.M., Streitlien, K., Barrett, D.S., and Triantafyllou, M.S. (1998). "Oscillating foils of high propulsive efficiency". *Journal of Fluid Mechanics*, 360, 41–72.
- Beardsley, C., Bergeron, L., McLean, A., Nguyen, K., Vu, M., Watson, C., Nayfeh, A., Shehata, H., Woolsey, C., and Hajj, M. (2018). A modular biolocomotion emulator for hydrodynamic testing in a towing tank. In *OCEANS* 2018 MTS/IEEE Charleston, 1–8. IEEE.
- Eloy, C. (2012). Optimal strouhal number for swimming animals. *Journal of Fluids and Structures*, 30, 205–218.
- Koochesfahani, M.M. (1989). Vortical patterns in the wake of an oscillating airfoil. *AIAA Journal*, 27(9), 1200–1205.
- Lauder, G.V. and Tytell, E.D. (2005). Hydrodynamics of undulatory propulsion. In *Fish Biomechanics*, volume 23 of *Fish Physiology*, 425–468. Academic Press.
- Lighthill, M.J. (1971). Large-amplitude elongated-body theory of fish locomotion. *Proceedings of the Royal Society of London. Series B, Biological Sciences*, 179(1055), 125–138.
- Maertens, A.P., Triantafyllou, M.S., and Yue, D.K.P. (2015). Efficiency of fish propulsion. *Bioinspiration & Biomimetics*, 10(4), 046013.
- Mason, R. and Burdick, J.W. (2000). Experiments in carangiform robotic fish locomotion. In *Proceedings* 2000 ICRA. Millennium Conference. IEEE International Conference on Robotics and Automation. Symposia Proceedings (Cat. No.00CH37065), volume 1, 428–435 vol 1
- Murray, M. and Howle, L. (2003). Spring stiffness influence on an oscillating propulsor. *Journal of Fluids and* Structures, 17(7), 915–926.
- Quinn, D.B., Lauder, G.V., and Smits, A.J. (2014). Scaling the propulsive performance of heaving flexible panels. Journal of fluid mechanics, 738, 250–267.
- Read, D., Hover, F., and Triantafyllou, M. (2003). Forces on oscillating foils for propulsion and maneuvering. Journal of Fluids and Structures, 17(1), 163–183.
- Theodorsen, T. and Mutchler, W.H. (1935). General theory of aerodynamic instability and the mechanism of flutter: by theodore theodorsen. *Journal of the Franklin Institute*, 219(6), 766–767.
- Triantafyllou, M.S., Triantafyllou, G.S., and Gopalkrishnan, R. (1991). Wake mechanics for thrust generation in oscillating foils. *Physics of Fluids A: Fluid Dynamics*, 3(12), 2835–2837.
- Triantafyllou, M.S., Triantafyllou, G.S., and Grosenbaugh, M.A. (1993). Optimal thrust development in oscillating foils with application to fish propulsion. *Journal of Fluids and Structures*, 7(2), 205–224.
- Tytell, E.D. and Lauder, G.V. (2004). The hydrodynamics of eel swimming. *Journal of Experimental Biology*, 207(11), 1825–1841.
- Webb, P.W. (1975). Hydrodynamics and energetics of fish propulsion. Bulletin of the fisheries research board of Canada, 190, 1–159.
- Weihs, D. (1989). Design features and mechanics of axial locomotion in fish. *American Zoologist*, 29(1), 151–160.